

Tuning Interfacial Thermal and Electrical Conductance across a Metal/MoS₂ Monolayer through *N*-Methyl-2-pyrrolidone Wet Cleaning


Yen-Ju Wu, Yann-Wen Lan,* Shih-Chieh Hsu, Chen-Hao Yeh, Yu-Seng Ku, Jyh-Chiang Jiang, and Yibin Xu*

Extensive effort is dedicated to developing 2D materials as an alternative to Si-based semiconductor technology. As the size decreases, heat dissipation at various interfaces becomes increasingly important in controlling device performance. On the other hand, the high interfacial thermal resistances can be applied for thermoelectric devices or thermal insulators by achieving ultralow thermal conductivity via nanostructuring. Here, it is found that a) the thermal and electrical conductance of the Au/MoS₂ monolayer interface can be tuned by changing the interfacial chemical properties through *N*-methyl-2-pyrrolidone (NMP) wet cleaning while preserving the MoS₂ structure; b) the effectiveness of the NMP cleaning process, which removes surface adsorbates, exhibits a temperature dependence; c) experimental results demonstrate that adequate oxygen adsorbates at the Au/MoS₂ interface significantly improve the thermal and electrical conductance, in agreement with the simulation results. The interfacial thermal conductance increases by 339.87% when oxygen adsorbates are partially removed and decreases by 74.37% as a sharp interface exists (oxygen adsorbates are removed) compared to the as-deposited interfaces. The electrical conductance shows up to 2 order increase after NMP cleaning. This finding can both enhance the heat dissipation in functional devices and provide new options for the interface design of thermal insulating thin films.

1. Introduction

2D materials have become attractive for overcoming the bottleneck that causes efficiency degradation in nanoscale electronic devices such as thin-film transistors,^[1] supercapacitors,^[2] and photodetectors^[3,4] as a result of reducing the particle size of bulk materials to the nanoscale. Compared with conventional bulk semiconductors such as Si, 2D materials have relatively high stability, dangling-bond-free surfaces, and ultrathin atomic-scale thickness. Here, the interface of Au and monolayer MoS₂ was chosen for investigation. Au is broadly used for electrodes with high stability under ambient conditions, whereas MoS₂ is a 2D material in the transition metal dichalcogenide (TMD) family. Because of its abundance, nontoxicity, and excellent electrical properties,^[1,5] MoS₂ has been widely studied. It can also be synthesized into large-area thin films. The high electrical contact resistance at the metal/2D material interface can be tuned

Dr. Y.-J. Wu
International Center for Young Scientists (ICYS)
National Institute for Materials Science (NIMS)
1-2-1 Sengen, Tsukuba, Ibaraki 305-0047, Japan
Dr. Y.-J. Wu, Dr. Y. Xu
Center for Materials research by Information Integration (CMI2)
Research and Service Division of Materials Data
and Integrated System (MaDIS)
National Institute for Materials Science (NIMS)
1-1 Namiki, Tsukuba, Ibaraki 305-0044, Japan
E-mail: Xu.Yibin@nims.go.jp

 The ORCID identification number(s) for the author(s) of this article can be found under <https://doi.org/10.1002/admi.202000364>.

© 2020 The Authors. Published by WILEY-VCH Verlag GmbH & Co. KGaA, Weinheim. This is an open access article under the terms of the Creative Commons Attribution License, which permits use, distribution and reproduction in any medium, provided the original work is properly cited.

The copyright line for this article was changed on 5 June 2020 after original online publication.

DOI: 10.1002/admi.202000364

Prof. Y.-W. Lan, Y.-S. Ku
Department of Physics
National Taiwan Normal University
88, Sec.4, Ting-Chou Rd., Taipei 11677, Taiwan
E-mail: ywlan@ntnu.edu.tw
Prof. S.-C. Hsu
Department of Chemical and materials Engineering
Tamkang University
No.151, Yingzhuang Rd., Tamsui Dist., New Taipei City 25137, Taiwan
Prof. C.-H. Yeh
Department of Materials Science and Engineering
Feng Chia University
No. 100, Wenhua Rd., Seatwen, Taichung 40724, Taiwan
Prof. C.-H. Yeh
First-Principles Simulation Group
Nano-Theory Field
International Center for Materials Nanoarchitectonics (WPI-MANA)
National Institute for Materials Science (NIMS)
1-1 Namiki, Tsukuba, Ibaraki 305-0044, Japan
Prof. C.-H. Yeh, Prof. J.-C. Jiang
Department of Chemical Engineering
National Taiwan University of Science and Technology
No.43, Keelung Rd., Sec.4, Da'an Dist., Taipei 10607, Taiwan

through phase or doping engineering.^[6–9] An ultrahigh vacuum (10^{-9} Torr) metal deposition process is suggested to ensure high interface quality at the metal/2D material junction, which yields a threefold increase in the electrical contact conductance.^[10]

Thermal management and heat transport at the metal/2D material interface have attracted less attention than electrical performance. Nevertheless, poor heat dissipation exacerbates the degradation of devices as their dimensionality is reduced. Interfacial heat transport is sensitive to the material structure and chemical bonding; therefore, vacancies, interstitial impurities, and adsorbates on the MoS₂ surface will affect the thermal conductance. To ensure uniformity and cleanliness of large-area semiconductor devices, a wet chemical cleaning process is commonly used. *N*-Methyl-2-pyrrolidone (NMP), which is used for cleaning and transferring 2D materials or layered materials via liquid-phase exfoliation, is a good hydrophilic solvent for enhancing the interfacial quality of metal/MoS₂.^[11–13] Lan and co-workers have reported that NMP cleaning can improve the electrical performance of monolayer MoS₂ field-effect transistors.^[14] However, whether NMP modifies the thermal properties of the metal/2D material interface is unclear.

MoS₂ is a promising thermoelectric material because of its unique density of states (DOS), which can enhance the Seebeck coefficient and result in a power factor as large as $8.5 \text{ mW m}^{-1} \text{ K}^{-2}$ for a bilayer MoS₂ variant at room temperature.^[15] Thermoelectric properties can be improved through phonon engineering,^[16] engineering of the strain effect,^[17] and introducing various dopants for p- and n-type materials.^[18,19] We previously proposed an interface design of inorganic composite thin films via machine learning and nanostructure optimization to achieve ultralow thermal conductivity for thermally insulating thin films or thermoelectric materials.^[20,21] The machine learning techniques can accelerate the material exploration for development^[22–24] and efficiency management of long-term control.^[25,26] This strategy holds promise for reducing the total thermal conductivity along the cross-plane direction via nanoengineering for metal/MoS₂ interfaces, which exhibit low thermal conductance. The metal can preserve the electrical conductance, and the metal/MoS₂ interfaces can impede heat transfer to ensure a low thermal conductivity.

Here, we demonstrate a tunable interfacial thermal and electrical conductance effect across a metal/MoS₂ monolayer using the NMP cleaning method. We used density functional theory (DFT) calculations to show that the amounts of oxygen adsorbates at the Au/MoS₂ interface affect the thermoelectric properties of the material: medium oxygen adsorbate contents (25–50%) correspond to materials with better thermal and electrical conductivities. Therefore, we used the NMP wet cleaning method to remove adsorbates at the Au/MoS₂ interfaces. We found that the cleaning efficiency of NMP is temperature dependent and that, remarkably, the experimental results agree with the simulation results. The atomic binding, structure, and tensile strain properties that affect the thermal and electrical conductance at the metal/MoS₂ monolayer interface were characterized by Raman spectroscopy, X-ray photoelectron spectroscopy (XPS), and transmission electron microscopy (TEM). The tunability of the thermal resistance was verified using frequency-domain thermoreflectance (FDTR),^[27] and

the device electrical resistance at the Au/MoS₂ interface was analyzed.

2. Results and Discussion

2.1. Simulation Results

The effect of different amounts of oxygen adsorbates or contaminants on the thermal and electrical conductance at the Au/MoS₂ interface were first analyzed via DFT calculations. The constructed unit cell of the Au/MoS₂ has a thickness of $\approx 1.9 \text{ nm}$; the unit cells with various oxygen percentages are shown in **Figure 1a**. Because the simulation is based on a periodic structure, which behaves more like a Au/MoS₂ composite, a direct comparison of the simulation and experimental values is not possible. However, the simulation results can be used to analyze the effect of various oxygen amounts on the thermal and electrical properties in the Au/MoS₂ systems. In order to easily analyze the simulated results, here, the relaxation time (τ) of all structures is assumed to be constant. We compared the tendency of thermal conductivity/relaxation time (κ/τ) and electrical conductivity/relaxation time (σ/τ), and the units are $\text{W m}^{-1} \text{ K}^{-1} \text{ s}^{-1}$ and $\Omega^{-1} \text{ m}^{-1} \text{ s}^{-1}$, respectively. The simulated κ/τ , σ/τ , and Seebeck coefficient versus temperature in the range from 100 to 500 K are shown in **Figure 1b–d**. The percentages of oxygen adsorbates (surface coverage) at the Au/MoS₂ interfaces are 0%, 25%, 50%, 75%, and 100%.

The κ/τ of all of the samples increases with increasing temperature, and the order of them is $25\% \text{ O} > 50\% \text{ O} > 75\% \text{ O} = 100\% \text{ O} > 0\% \text{ O}$ at temperatures greater than 300 K, as shown in **Figure 1b**. The residual oxygen adsorbates after the 50°C NMP cleaning play an important role in modifying the interface region, resulting in better phonon transport. The σ/τ in all samples with different O percentages decreases with increasing temperature, as shown in **Figure 1c**. All of the energy bandgaps of the MoS₂ monolayers with O adsorbates on their surface decrease compared with the energy bandgap of the as-deposited MoS₂. In addition, the overlap of DOS between MoS₂ and Au decreases with increasing oxygen percentage. The detailed electron DOS of the MoS₂ monolayer and the Au/MoS₂ interfaces can be found in **Figure S2** (Supporting Information). The order of σ/τ at temperatures greater than 300 K is $25\% \text{ O} > 50\% \text{ O} > 100\% \text{ O} \approx 75\% \text{ O} > 0\% \text{ O}$. These results indicate that adequate oxygen would improve the thermal and electrical conductance but might also increase the interfacial vacancies or roughness in a real experimental procedure, both of which need to be carefully controlled.

The simulated Seebeck coefficient does not exhibit strong temperature dependence at temperatures greater than 300 K in **Figure 1d**. The samples with adsorbate contents of 0% O and 50% O exhibit p-type characteristics, whereas those with adsorbate contents of 75% O and 100% O exhibit n-type characteristics; the samples with 25% O undergo a conversion from p- to n-type at temperatures greater than 300 K. We had performed some experiments related to the conversion from n- to p-type in MoS₂ and other TMDs, and the conversion could be controlled by oxide layers,^[28] the doping via implantation technique,^[29] and electron-beam irradiation.^[30] The oxygen doping

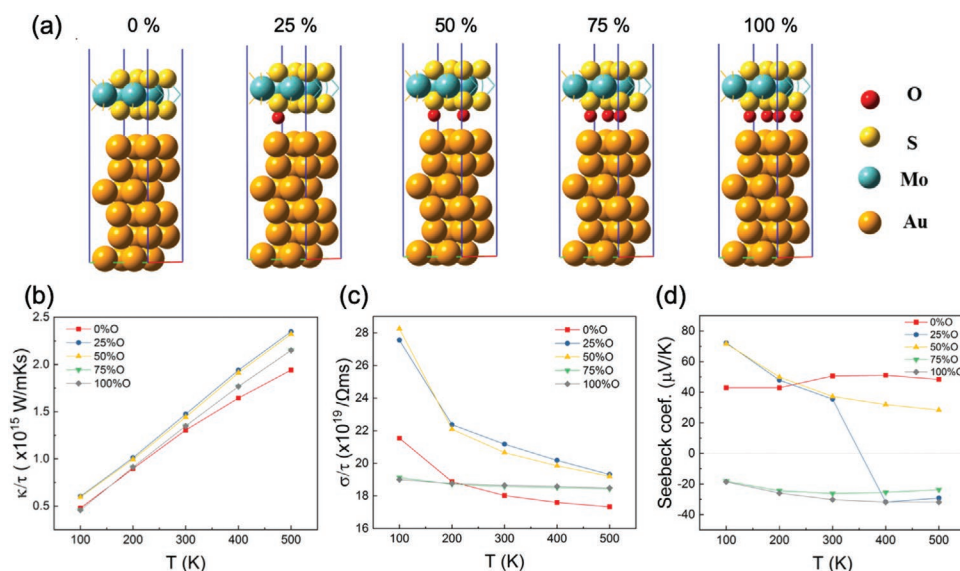


Figure 1. a) Unit cells of Au/MoS₂ with different oxygen atom contents of 0%, 25%, 50%, 75%, and 100% (surface coverage). The simulated structure is composed of periodic unit cells separated by a 15 Å vacuum spacing to ensure no interactions between the Au/MoS₂ composites. The simulated b) κ/τ , c) σ/τ , and d) Seebeck coefficient of a Au/MoS₂ monolayer (at different percentages of oxygen adsorbates) versus NMP temperatures. For comparison with the experimental results, the simulated samples with 75–100% O correspond to the as-deposited MoS₂, those with 25–50% O correspond to the 50 °C NMP-cleaned MoS₂, and those with 0% O correspond to the 110 °C NMP-cleaned MoS₂. The sample with intermediate oxygen adsorbates (25–50%) shows optimized thermal and electrical conductance.

is one of commonly used methods to achieve the conversion. According to our experiences, we simulated the oxygen content at Au/MoS₂ interfaces and predicted the Seebeck coefficient at different temperatures, as can be seen in Figure 1d. The Seebeck coefficient of the p-type samples is slightly greater than that of the n-type samples. The order of Seebeck coefficients at temperatures less than 200 K is 25% O \approx 50% O > 0% O > 75% O \approx 100% O, whereas the 0% O samples exhibit the highest Seebeck coefficient at temperatures greater than 300 K. Thus, higher Seebeck coefficients were achieved with oxygen adsorbates at temperatures less than 200 K. These simulation results suggest that residual (adequate) oxygen adsorbates at the interface would provide better thermal and electrical conductivities. Next, we will analyze the experimentally determined thermal and electrical conductivity results.

2.2. Characterization

We assessed the quality of our large-area monolayer MoS₂ films using Raman spectroscopy. **Figure 2a** shows the Raman spectra of the MoS₂ monolayer before (dotted line) and after (solid line) the NMP chemical treatment at different temperatures. To exclude the position effect, the Raman spectra were recorded at the same location on each sample before and after the NMP cleaning. The two characteristic peaks at ≈ 381 and ≈ 403 cm⁻¹ correspond to the in-plane vibration (E_{2g}^1) of the Mo and S atoms and to the out-of-plane vibration (A_{1g}) of the S atoms, as displayed in Figure 2a, respectively. The A_{1g} peak of the sapphire substrate, which was used to align the data, also appears at 414 cm⁻¹ in the spectra of all of the samples. The frequency difference ($\Delta\omega$) between the E_{2g}^1 and A_{1g} modes of MoS₂ is ≈ 21 – 22 cm⁻¹, which is slightly greater than previously reported

values of 18–20 cm⁻¹ for MoS₂ monolayers.^[31–33] However, the characteristic peaks and $\Delta\omega$ not only depend on the layer number but also on the applied laser wavelength, position, and synthesis method (e.g., chemical vapor deposition (CVD) or exfoliation).^[32] The precise estimation of the MoS₂ thickness was further confirmed by TEM images presented later in this section. In all samples shown in Figure 2a, the characteristic peaks do not exhibit a substantial change in frequency or intensity after the NMP cleaning at temperatures ranging from 25 to 110 °C, indicating that the MoS₂ structure remained intact after the NMP cleaning.

The Raman spectra of MoS₂ coated with 5 nm thick Au are shown in Figure 2b. The Raman signal from the Au/MoS₂ interfaces is still visible in the spectra of the samples with a 5 nm Au layer but not in the spectra of the samples with 150 nm thick Au layer, which were used for the FDTR measurements. Compared with the spectrum of the as-deposited MoS₂ without Au (green curve in Figure 2b), that of the Au-coated sample shows a split of the characteristic peak of the E_{2g}^1 mode into two peaks at 375.44 and 381.82 cm⁻¹ ($\Delta\omega \approx 6$ cm⁻¹), whereas the A_{1g} mode shows no clear shift. A similar redshift ($\Delta\omega$) has been reported for separated peaks at 6.6 and 6.38 cm⁻¹ in the spectra of Au/Ti/MoS₂ and Au/MoS₂ interfaces.^[34,35] The tensile strain induced by the lattice mismatch of Au and MoS₂ causes the redshift of the E_{2g}^1 mode, whereas the interfacial bonding variation induced by Au deposition is negligible. Nevertheless, the peak intensity of the out-of-plane vibration (A_{1g}) slightly decreases when the sample temperature during the NMP cleaning process is increased, as shown in Figure 2b, implying that the interfacial bonding of Au/MoS₂ might be weakened by NMP cleaning.

MoS₂ samples were analyzed by XPS after being transferred from sapphire to Au substrates to prevent interference from the oxygen atoms of the sapphire substrate. The XPS results in

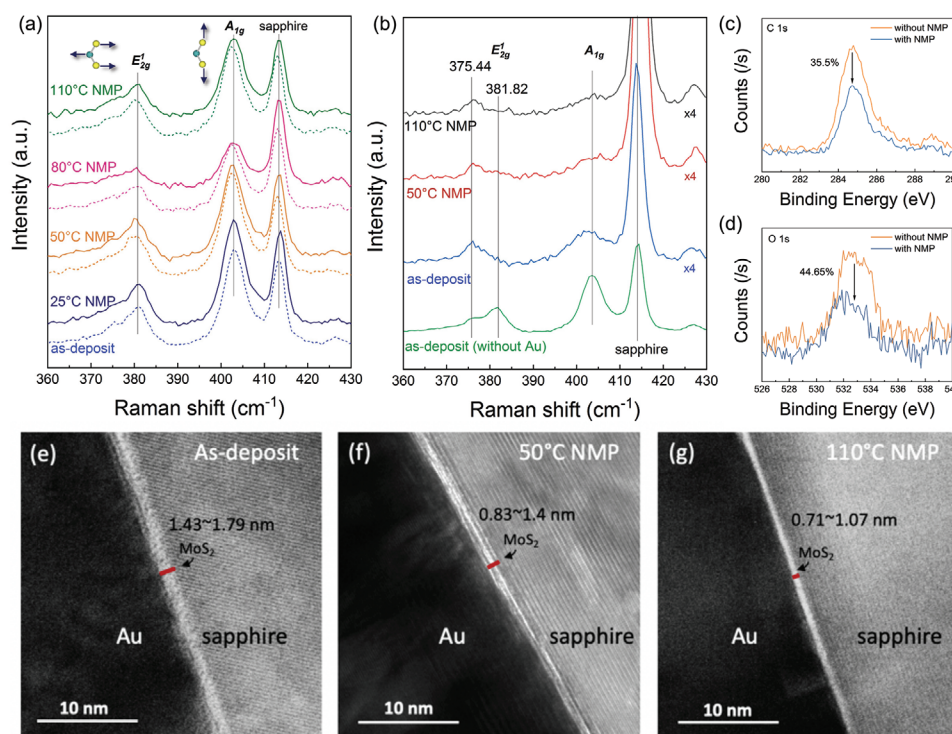


Figure 2. a) Raman spectra of the MoS₂ monolayer of the as-deposited, 25, 50, 80, and 110 °C NMP-cleaned devices. The Raman spectra were recorded at the same position before and after NMP cleaning; these spectra are represented by dotted and solid lines, respectively. The yellow and green atoms of the vibration modes (E_{2g}^1 and A_{1g}) represent the S and Mo atoms, respectively. The characteristic peaks do not change after the NMP cleaning process at various temperatures. b) The Raman spectra of an MoS₂ monolayer with 5 nm Au top layer. The as-deposited MoS₂ and the 50 and 110 °C NMP-cleaned MoS₂ are represented by blue, red, and black curves, respectively. The spectrum of the as-deposited MoS₂ without the Au top layer is indicated by a green curve and is provided for reference. The observed redshift of the E_{2g}^1 mode is due to the tensile strain induced by the lattice mismatch between Au and MoS₂. The decrease in intensity of the A_{1g} mode is attributed to the lower interfacial bonding at the Au/MoS₂ interface. The XPS spectra for the c) C 1s and d) O 1s core peaks of the MoS₂ sample transferred onto a Au substrate with and without NMP cleaning. The carbon and oxygen contents decrease by 35.5% and 44.65% after NMP cleaning. TEM images of the Au/MoS₂ monolayer/sapphire substrate, where the MoS₂ layer is e) as-deposited, f) 50 °C NMP-cleaned, and g) 110 °C NMP-cleaned. The interfacial region decreases after NMP cleaning, as revealed by a comparison of the (e) as-deposited sample with a thicker interfacial region and the (g) 110 °C NMP-cleaned sample with the sharpest Au/MoS₂ interface.

Figure 2c reveal that the carbon and oxygen contents decrease by 35.5% and 44.65%, respectively, after the 110 °C NMP cleaning. At the same time, the Mo_{3d} , S_{2s} , Mo_{3p} , and S_{2p} binding energies show no obvious variations (details are available in Figure S3 in the Supporting Information). These results imply that the NMP cleaning can effectively remove the undesirable adsorbates or contaminants from the surface while not affecting the physical properties of the MoS₂. The effect of the NMP residue or the adsorbates on the transfer the samples from the sapphire substrate to the Au substrate can be excluded; details are available elsewhere.^[14]

The lattice structure of the Au/MoS₂/sapphire interfaces was characterized by TEM, as shown in Figure 2e–g. A broad and mixed interfacial region at the Au/as-deposited MoS₂ interface with a thickness of 1.43–1.79 nm of MoS₂ is shown in Figure 2e. The interface of the Au/110 °C NMP-cleaned MoS₂ in Figure 2g is smooth and clear and the thickness of MoS₂ is 0.71–1.07 nm, which is exactly the monolayer thickness of MoS₂. The Au/50 °C NMP-cleaned MoS₂ in Figure 2f shows intermediate thickness (0.83–1.4 nm) and interfacial cleanness compared with the interfaces in Figure 2e,g. This comparison shows that the NMP cleaning can eliminate the adsorbates from the MoS₂ surface, consistent with the XPS results, and that the efficiency

of cleaning increases with increasing temperature. In addition, the adsorbates or contaminants on the as-deposited MoS₂ surface form a mixed region at the interface of Au and MoS₂. The extra oxygen (or carbon) will likely form new bonds such as O–S and Au–O at the Au/MoS₂ interface, corresponding to the intensity change of A_{1g} in Figure 2b. The change in the chemical characteristics at the Au/MoS₂ interfaces will affect the thermal and electrical transport across the interfaces.

2.3. Thermal Properties

The total thermal conductance of Au/MoS₂/sapphire is plotted in Figure 3a as a function of the NMP cleaning temperature. The thermal conductance shown in Figure 3a was evaluated on the basis of the reciprocal of the total thermal resistance in Figure S1 (Supporting Information). The Au surface was heated by a 405 nm pump laser, and the thermoreflectance was detected by a 635 nm probe laser, as shown in Figure 3b. The thermal conductance at different NMP temperatures are listed in Table 1. The oxygen percentage of the as-deposited interface is assumed as 100% and that of other interfaces decreases as NMP temperatures increase. According to the

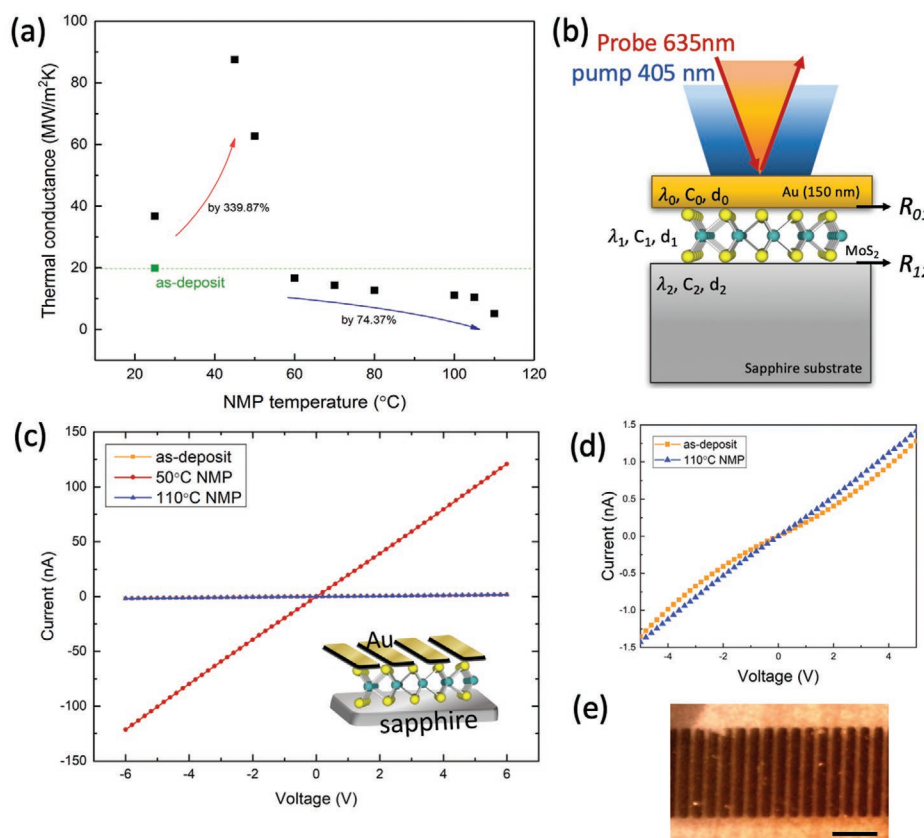


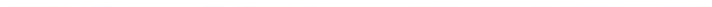
Figure 3. a) Total thermal conductance of the Au/MoS₂/sapphire interface versus NMP cleaning temperature from 25 to 110 °C. The thermal conductance increased by 339.87% after 45 °C NMP cleaning and conversely decreased by 74.37% after 110 °C NMP cleaning. The as-deposited sample is marked in green, whereas the green dashed line is used for comparing the thermal conductance with that of the as-deposited sample. b) Schematic of the thermal conductance measurement of Au/MoS₂ monolayer on the sapphire substrate (see the details of the 1D heat conduction equation in the Experimental Section (Experimental Methods)). c) *I*–*V* curves of the as-deposited MoS₂ and MoS₂ that was subjected to 50 and 110 °C NMP cleaning. The 50 °C NMP cleaning dramatically improves (decreases) the contact resistance. The bottom illustration shows the measured samples with patterned Au pads corresponding to the photo in (e). d) *I*–*V* curves of the as-deposited MoS₂ and the 50 °C NMP-cleaned MoS₂. Linear *I*–*V* curves are observed after the NMP cleaning. e) The patterned Au pad of the 50 °C NMP-cleaned sample (the scale bar represents 1 mm).

positive correlation between cleaning efficiency and NMP temperature discussed above (Figure 2c–g), the simulated samples in Figure 1a with 75–100% O can be represented as the as-deposited MoS₂, those with 25–50% O as the 45–50 °C NMP-cleaned MoS₂, and those with 0% O as the 110 °C NMP-cleaned MoS₂.

The total thermal conductance of the sample with the as-deposited MoS₂ was 19.89 MW m^{−2} K^{−1}. The relatively low thermal conductance of metal/MoS₂ interfaces indicates that

such interfaces present a bottleneck in heat dissipation.^[36] When the NMP cleaning temperature was increased to 45 °C, the thermal conductance increased by 3.39 times, to 87.49 MW m^{−2} K^{−1}. This increase in thermal conductance is attributed to the removal of undesirable adsorbates on the MoS₂ surface by the NMP cleaning process. However, when the cleaning temperature was increased to greater than 50 °C, the thermal conductance became lower than that of the as-deposited sample, decreasing by 74.37% to 5.12 MW m^{−2} K^{−1} at an

Table 1. The thermal conductance of the Au/MoS₂ monolayer under different NMP cleaning temperatures. The as-deposited interface is assumed to have the most oxygen adsorbates at the interface, and the oxygen percentage decreases with increasing the NMP temperatures corresponding to the TEM images in Figure 2e–g.

O percentage [%] at the interface	100										0
NMP temperature [°C]	As-deposited	25	45	50	60	70	80	100	105	110	
Thermal conductance [MW m ⁻² K ⁻¹]	19.89	36.76	87.49	62.70	16.65	14.39	12.68	11.11	10.46	5.12	

NMP cleaning temperature of 110 °C. As the TEM images in Figure 2g show, a smooth and clean Au/MoS₂ interface can be achieved through NMP cleaning at 110 °C; however, the phonon density of states (PDOS) of Au and MoS₂ have a large mismatch above 5 THz that remarkably hinders the heat transport and leads to low interfacial thermal conductance.^[37]

The high thermal conductance of the 50 °C NMP-cleaned sample, whose TEM image is presented in Figure 2f, implies that adsorbates such as oxygen may increase the overlap region of the PDOS between Au and MoS₂. Zhan et al. have reported that the PDOS is modified in the interface regions, resulting in a better match than in the bulk region.^[38] Hahn et al. proposed a thermal conductance analysis of Si/Ge interfaces with mixed regions by molecular dynamics simulations; their results showed that, compared with the sharp interface, the 0.5 nm mixed region exhibited increased thermal conductance, whereas a larger mixed region (1 or 2 nm) exhibited lowered thermal conductance.^[39] Accordingly, there would be a trade-off to enhancing the thermal conductance across the Au/MoS₂ interfaces: the broad mixed region (Figure 2e) and sharp interface (Figure 2g) both adversely affect thermal transport, and the intermediate interface (Figure 2f) has optimized thermal conductance. That is, the thermal conductivity of the Au/50 °C NMP-cleaned MoS₂ is greater than that of the Au/110 °C NMP-cleaned MoS₂, whereas the Au/as-deposited MoS₂ exhibits the lowest thermal conductivity, in good agreement with the simulation results in Figure 1b.

2.4. Electrical Characterization

Figure 3c shows the current–voltage (*I*–*V*) curves of the as-deposited, 50 °C NMP-cleaned, and 110 °C NMP-cleaned samples. Multiple devices with the same channel length between two electrodes for each of the three cases were used to check the consistency and reproducibility of the results. A representative device is shown in Figure 3e. Note that the *I*–*V* curves change substantially from nonlinear to linear after the NMP cleaning, as shown in Figure 3d, indicating that ohmic-like behavior appears only after NMP cleaning. This result was reproducibly measured in different devices, demonstrating high consistency. Furthermore, the total electrical resistance was dramatically reduced by ≈2 orders of magnitude (from 3910 to 50 MΩ) by the 50 °C NMP cleaning, which is attributed to the improvement of contact resistance at the Au/MoS₂ interface. Higher contents of adsorbates such as O and C on the as-deposited sample may cause impurity scattering, adversely affecting the electron transport. However, the residual adsorbates after 50 °C NMP cleaning (Figure 2f) enhance the electron transport at the Au/MoS₂ interface compared with that at the sharp interface of the 110 °C NMP-cleaned sample (Figure 2g). Several authors have proposed improving contact through surface treatment or surface engineering via interfacial chemical conditioning. Houssa et al. reported a large discrepancy in contact resistance of the MoS₂-based metal/semiconductor heterojunctions by considering the interaction of 1T-MoS₂ with various chemical species (hydrogen, oxygen). The atoms or molecules of these species lower the work function of the 1T-MoS₂ during the local transformation, leading to low contact resistances.^[40] Leong

et al. reported that the presence of zigzag edges on nickel–graphene electrodes enhances electrical contact via a tunneling effect and lower work function.^[41] Bhattacharjee et al. found that applying a sulfur-based (ammonium sulfide) treatment to MoS₂ could reduce its contact resistance and variability with high-work-function metals.^[42] The similar chemical enhancement at interfaces of metal/graphene has been applied as well to increase the performance for sensitive surface detection^[43] and surface-enhanced Raman spectroscopy.^[44] The charge transport can be tuned by the degree of interaction between the metal and TMD layer via interlayers, doping strategy, or defect engineering.^[4,45,46] The interlayer between the material and metal electrode (buffer layer) which plays a role for carrier transport has also been used for thin film solar cells,^[47] and the bandgap alignment and the carrier concentration at donor or acceptor level are essential for the interfacial conductive characteristics.

Neither the broad interfacial region of the as-deposited sample nor the sharp interface of the 110 °C NMP-cleaned sample were optimized interfaces for electrical contacts from our electrical measurement, although the 110 °C NMP cleaning process provided MoS₂ with ohmic-like contact (linear *I*–*V* characteristics). That is, the Au/50 °C NMP-cleaned MoS₂ interface exhibited better electrical conductivity than the Au/110 °C NMP-cleaned MoS₂ and the Au/as-deposited MoS₂, which is consistent with the simulated electrical conductivity results in Figure 1c. The intermediate interfaces of the 45–50 °C NMP-cleaned samples, which exhibit high thermal conductance and low electrical contact resistance, have strong potential for use in high-performance transistors on MoS₂ or other TMD materials. On the other hand, the 110 °C NMP-cleaned Au/MoS₂ interface, which exhibits low thermal conductance and good electrical contact, can be a good candidate for thermoelectric composites via interface nanoengineering.

3. Conclusion

We proposed an effective and simple NMP cleaning method for tuning the thermal and electrical conductance at the Au/MoS₂ interface. The thermal conductance can be increased by 3.39 times by increasing the wet cleaning temperature by ≈45–50 °C; on the other hand, it decreases by 74.37% when the cleaning temperature is increased to 110 °C. The total electrical resistance can be reduced by 2 orders of magnitude when the NMP cleaning is performed at 50 °C. We found that the ability of the NMP cleaning procedure to remove undesirable adsorbates from the MoS₂ surface while preserving the physical properties of the material is temperature dependent. The Au/MoS₂ interface changed from a broad and mixed interfacial region to a cleaner and thinner region when the cleaning was conducted at 50 °C and changed gradually to a sharp interface as the NMP cleaning temperature was increased at 110 °C. The intermediate interfacial region at the Au/MoS₂ interface (45–50 °C NMP-cleaned) exhibited excellent interfacial thermal conductance and the lowest electrical contact resistance among the investigated samples. The experimental results are in good agreement with the simulated results, indicating that adequate oxygen adsorbates at the Au/MoS₂ interface enhance the thermal and

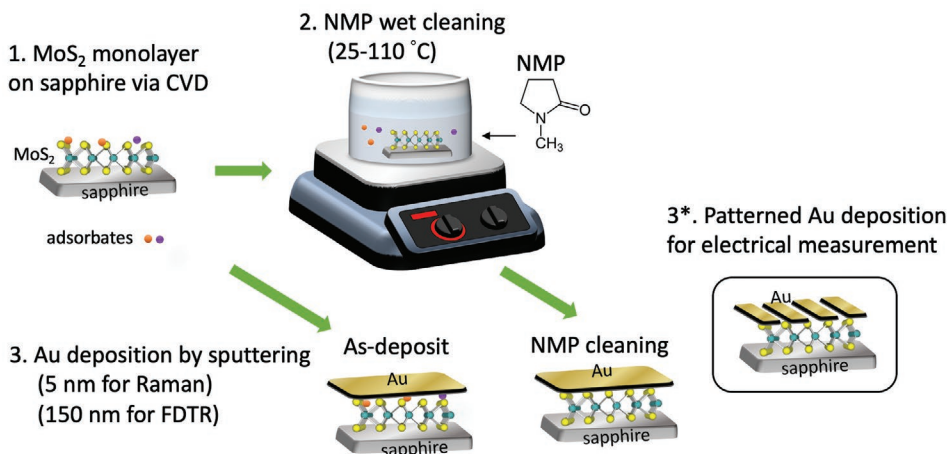


Figure 4. The workflow of the NMP cleaning process on MoS₂ samples. The thickness and pattern of the deposited Au layers were varied depending on the measurement technique for which the sample was prepared (Raman, FDTR, or electrical measurement).

electrical conductance. We have shown that the interfacial thermal and electrical conductance of Au/MoS₂ can be tuned by changing the interfacial chemical properties via NMP wet cleaning, which is promising for both enhancing the heat dissipation of functional ultrascaled electronics and for interface design of thermal insulating thin films.

4. Experimental Section

Experimental Methods: The continuous monolayer MoS₂ films were grown on sapphire substrates via CVD in a hot-wall furnace by sulfuring MoO₃ powders at 750 °C. The sulfur stream was generated by heating sulfur powder at 190 °C under an Ar carrier gas. The sapphire substrate was placed downstream at the center of the furnace. The sample was immersed into NMP solution for 20 min at various temperatures from 25 to 110 °C. All samples were rinsed with isopropyl alcohol (IPA) to remove any residual chemical species from their surface, and they were subsequently dried under blown nitrogen gas. The samples were placed in a vacuum chamber for Au deposition followed by NMP cleaning within 30 min via sputtering (CFS-4EP-LL, 5×10^{-4} Pa). Samples with 5 and 150 nm thick Au layers were used for the Raman spectroscopy and thermal property measurements, respectively. Meanwhile, a metal mask with a lateral size of 200 $\mu\text{m} \times 2$ mm was used to deposit 100 nm Au pads using an electron beam evaporator (EIKO, 5×10^{-5} Pa) for electrical measurement purposes. The detailed flow of the NMP wet cleaning process for MoS₂ samples is shown in Figure 4.

For the XPS measurements, the MoS₂ monolayer was transferred onto a Au substrate from the sapphire substrate to avoid interference from the oxygen signals of the oxide substrate. Raman spectra were collected with a micro-Raman spectrometer (HORIBA-JOBIN-YVON, model T64000) with low-frequency (<200 cm⁻¹) capability; the spectrometer was equipped with a single-mode laser with a wavelength of 514 nm. The thermal resistances of the Au/MoS₂ monolayer/sapphire structures were measured under vacuum (<0.02 Pa) at room temperature using the FDTR method. The Au film layer functioned as a transducer heated by a pump laser with a certain angular frequency. The pump laser was a multimode diode laser with a wavelength of 405 nm (360 mW) modulated by a lock-in amplifier (Stanford SR8300). The temperature response at the surface of the Au film was measured by a probe laser with a wavelength of 635 nm (5 mW). Measurements were carried out at three positions on each sample at four frequencies from 1 to 8 kHz for greater accuracy and stability. Schematics of the fabricated structure and the measurement technique are shown in Figure 3b. The

temperature at the Au surface, $T(0)$, was obtained using the 1D heat conduction equation^[38,48–51]

$$\frac{T(0)}{qd_0} = \frac{e^{-\frac{\pi}{4}}}{\sqrt{2\omega\lambda_2 C_2}} + R_{01} + R_{12} + \left(1 - \frac{\lambda_0 C_0}{\lambda_2 C_2}\right) \frac{d_0}{\lambda_0} + \left(1 - \frac{\lambda_1 C_1}{\lambda_2 C_2}\right) \frac{d_1}{\lambda_1} \quad (1)$$

where q is the heat flux, d is the film thickness, ω is the frequency, λ is the thermal conductivity, C is the volumetric heat capacity, and the subscripts 0, 1, and 2 refer to the Au, MoS₂ monolayer, and the sapphire substrate, respectively; R_{01} and R_{12} are the interfacial thermal resistance of the Au/MoS₂ and the MoS₂/sapphire, respectively, as shown in Figure 3b. The fourth and fifth terms in Equation (1) represented the thermal resistance of the Au and MoS₂ monolayer, respectively. The total thermal resistance could be evaluated by the sum of the second to fifth terms in Equation (1), which was the intercept of the linear plot of $\frac{T(0)}{qd_0}$ versus $\frac{1}{\sqrt{\omega}}$ obtained from the measurement. In this work, the total thermal conductance in various samples was calculated by the reciprocal of the total thermal resistance. The measured thermal resistance with experimental standard deviation is provided in Figure S1 (Supporting Information).

Simulation Procedure: All DFT calculations were performed using the Vienna Ab-initio Simulation Package.^[52–55] The projector-augmented-wave method^[56,57] was used in conjunction with the generalized gradient approximation and Perdew–Burke–Ernzerhof^[58] exchange–correlation functional. The Kohn–Sham orbitals were expanded in a plane-wave basis set with a kinetic energy cutoff of 500 eV. The convergence threshold was set to 10⁻⁵ eV for the total electronic energy in the self-consistent loop. The atomic positions were relaxed using the quasi-Newton algorithm until the x -, y -, and z -components of the unconstrained atomic force were smaller than 1×10^{-2} eV Å⁻¹.

The calculated lattice constants for the bulk Au and MoS₂ unit cells were 4.15 and 3.18 Å, respectively, in good agreement with the experimental values.^[59,60] In the Au/MoS₂ composites, the Au(111) surface was adopted, which was modeled by a six-layer slab within a (2 × 2) lateral supercell, where the lowest three layers were fixed; the MoS₂ sheet was also modeled in a (2 × 2) lateral supercell. The lattice mismatch of the Au/MoS₂ composites was controlled to be smaller than 3%. For the summation in the Brillouin zone, the Monkhorst–Pack mesh k -point^[61] was set to (8 × 8 × 8), (8 × 8 × 1), and (4 × 4 × 1) for the Au(111) surface, MoS₂ unit cell, and Au/MoS₂ composites, respectively. The composites were separated with a vacuum spacing of 15 Å to ensure no interactions occurred between them. In addition, oxygen adsorption (surface coverage) of 25–100% was carried out on the MoS₂ sheet to represent various oxygen concentrations in the experiment. Each oxygen

atom was adsorbed onto each top site of the sulfur atoms, resulting in the most stable structures, as shown in Figure 1a. The thermoelectric properties were calculated using the BoltzTraP code,^[62] which adopted the constant relaxation time and rigid band approximations via the semiclassical Boltzmann transport theory.

Supporting Information

Supporting Information is available from the Wiley Online Library or from the author.

Acknowledgements

This work was supported by the “Materials Research by Information Integration” Initiative (MI2I) project of the Support Program for Starting Up Innovation Hub from Japan Science and Technology Agency (JST). The National Center of High-Performance Computing (NCHC) contributed to this project by allowing access to their computer facilities and donating computer time.

Conflict of Interest

The authors declare no conflict of interest.

Keywords

electrical conductance, interfacial thermal resistances, molybdenum disulfide, monolayers, wet cleaning

Received: February 28, 2020
Revised: April 11, 2020
Published online:

- [1] J. Pu, Y. Yomogida, K. K. Liu, L. J. Li, Y. Iwasa, T. Takenobu, *Nano Lett.* **2012**, *12*, 4013.
- [2] K. Wang, L. Li, W. Xue, S. Zhou, Y. Lan, H. Zhang, Z. Sui, *Int. J. Electrochem. Sci.* **2017**, *12*, 8306.
- [3] M. Tan, Y. Hao, X. Ren, *J. Electron. Mater.* **2014**, *43*, 3098.
- [4] Q. Cheng, J. Pang, D. Sun, J. Wang, S. Zhang, F. Liu, Y. Chen, R. Yang, N. Liang, X. Lu, Y. Ji, J. Wang, C. Zhang, Y. Sang, H. Liu, W. Zhou, *InfoMat* **2020**, *2*, 656.
- [5] K. F. Mak, C. Lee, J. Hone, J. Shan, T. F. Heinz, *Phys. Rev. Lett.* **2010**, *105*, 136805.
- [6] L. Yang, K. Majumdar, H. Liu, Y. Du, H. Wu, M. Hatzistergos, P. Y. Hung, R. Tieckelmann, W. Tsai, C. Hobbs, P. D. Ye, *Nano Lett.* **2014**, *14*, 6275.
- [7] R. Kappera, D. Voiry, S. E. Yalcin, B. Branch, G. Gupta, A. D. Mohite, M. Chhowalla, *Nat. Mater.* **2014**, *13*, 1128.
- [8] K. A. Duerloo, Y. Li, E. J. Reed, *Nat. Commun.* **2014**, *5*, 4214.
- [9] D. Jena, K. Banerjee, G. H. Xing, *Nat. Mater.* **2014**, *13*, 1076.
- [10] C. D. English, G. Shine, V. E. Dorgan, K. C. Saraswat, E. Pop, *Nano Lett.* **2016**, *16*, 3824.
- [11] V. Kaushik, S. H. Wu, H. Jang, J. Kang, K. Kim, J. W. Suk, *Nanomaterials* **2018**, *8*, 587.
- [12] X. Cui, C. Z. Zhang, R. Hao, Y. L. Hou, *Nanoscale* **2011**, *3*, 2118.
- [13] Y. Xu, H. Cao, Y. Xue, B. Li, W. Cai, *Nanomaterials* **2018**, *8*, 942.
- [14] P.-C. Chen, C.-P. Lin, C.-J. Hong, C.-H. Yang, Y.-Y. Lin, M.-Y. Li, L.-J. Li, T.-Y. Yu, C.-J. Su, K.-S. Li, Y.-L. Zhong, T.-H. Hou, Y.-W. Lan, *Nano Res.* **2019**, *12*, 303.
- [15] K. Hippalgaonkar, Y. Wang, Y. Ye, D. Y. Qiu, H. Zhu, Y. Wang, J. Moore, S. G. Louie, X. Zhang, *Phys. Rev. B* **2017**, *95*, 115407.
- [16] Z. Jin, Q. Liao, H. Fang, Z. Liu, W. Liu, Z. Ding, T. Luo, N. Yang, *Sci. Rep.* **2015**, *5*, 18342.
- [17] J. X. Xiang, R. N. Ali, Y. F. Yang, Z. Zheng, B. Xiang, X. D. Cui, *Phys. E* **2019**, *109*, 248.
- [18] S. Kong, T. M. Wu, M. Yuan, Z. W. Huang, Q. L. Meng, Q. K. Jiang, W. Zhuang, P. Jiang, X. H. Bao, *J. Mater. Chem. A* **2017**, *5*, 2004.
- [19] S. Kong, T. Wu, W. Zhuang, P. Jiang, X. Bao, *J. Phys. Chem. B* **2018**, *122*, 713.
- [20] D. Wu, L. Xie, X. Chao, Z. Yang, J. He, *ACS Appl. Energy Mater.* **2019**, *2*, 1616.
- [21] Y.-J. Wu, M. Sasaki, M. Goto, L. Fang, Y. Xu, *ACS Appl. Nano Mater.* **2018**, *1*, 3355.
- [22] Y.-J. Wu, L. Fang, Y. Xu, *npj Comput. Mater.* **2019**, *5*, 56.
- [23] T. Zhang, L. Fang, Y. Xu, *Sci. Rep.* **2017**, *7*, 7109.
- [24] Y.-J. Wu, T. Zhan, Z. Hou, L. Fang, Y. Xu, *Sci. Data* **2020**, *7*, 36.
- [25] Y. Zhou, Y. Huang, J. Pang, K. Wang, *J. Power Sources* **2019**, *440*, 227149.
- [26] Y. Zhou, Y. Wang, K. Wang, L. Kang, F. Peng, L. Wang, J. Pang, *Appl. Energy* **2020**, *260*, 114169.
- [27] R. Kato, Y. Xu, M. Goto, *Jpn. J. Appl. Phys.* **2011**, *50*, 106602.
- [28] C.-Y. Lin, K. B. Simbulan, C.-J. Hong, K.-S. Li, Y.-L. Zhong, Y.-K. Su, Y.-W. Lan, *Nanoscale Horiz.* **2020**, *5*, 163.
- [29] Y.-W. Lan, P.-C. Chen, Y.-Y. Lin, M.-Y. Li, L.-J. Li, Y.-L. Tu, F.-L. Yang, M.-C. Chen, K.-S. Li, *Nanoscale Horiz.* **2019**, *4*, 683.
- [30] C.-P. Lin, P.-C. Chen, J.-H. Huang, C.-T. Lin, D. Wang, W.-T. Lin, C.-C. Cheng, C.-J. Su, Y.-W. Lan, T.-H. Hou, *ACS Appl. Electron. Mater.* **2019**, *1*, 684.
- [31] D. Dumcenco, D. Ovcinnikov, K. Marinov, P. Lazic, M. Gibertini, N. Marzari, O. Lopez Sanchez, Y. C. Kung, D. Krasnozhan, M. W. Chen, S. Bertolazzi, P. Gillet, A. Fontcuberta i Morral, A. Radenovic, A. Kis, *ACS Nano* **2015**, *9*, 4611.
- [32] B. M. Foley, S. C. Hernandez, J. C. Duda, J. T. Robinson, S. G. Walton, P. E. Hopkins, *Nano Lett.* **2015**, *15*, 4876.
- [33] Y. Liu, H. Nan, X. Wu, W. Pan, W. Wang, J. Bai, W. Zhao, L. Sun, X. Wang, Z. Ni, *ACS Nano* **2013**, *7*, 4202.
- [34] H. Yuan, G. Cheng, L. You, H. Li, H. Zhu, W. Li, J. J. Kopanski, Y. S. Obeng, A. R. Hight Walker, D. J. Gundlach, C. A. Richter, D. E. Ioannou, Q. Li, *ACS Appl. Mater. Interfaces* **2015**, *7*, 1180.
- [35] C. Gong, C. Huang, J. Miller, L. Cheng, Y. Hao, D. Cobden, J. Kim, R. S. Ruoff, R. M. Wallace, K. Cho, X. Xu, Y. J. Chabal, *ACS Nano* **2013**, *7*, 11350.
- [36] E. Yalon, O. B. Aslan, K. K. H. Smithe, C. J. McClellan, S. V. Suryavanshi, F. Xiong, A. Sood, C. M. Neumann, X. Xu, K. E. Goodson, T. F. Heinz, E. Pop, *ACS Appl. Mater. Interfaces* **2017**, *9*, 43013.
- [37] X. Liu, G. Zhang, Y.-W. Zhang, *Nano Res.* **2016**, *9*, 2372.
- [38] T. Zhan, S. Minamoto, Y. Xu, Y. Tanaka, Y. Kagawa, *AIP Adv.* **2015**, *5*, 047102.
- [39] K. R. Hahn, M. Puligheddu, L. Colombo, *Phys. Rev. B* **2015**, *91*, 195313.
- [40] M. Houssa, K. Iordanidou, A. Dabral, A. Lu, G. Pourtois, V. Afanasiev, A. Stesmans, *ACS Appl. Nano Mater.* **2019**, *2*, 760.
- [41] W. S. Leong, X. Luo, Y. Li, K. H. Khoo, S. Y. Quek, J. T. Thong, *ACS Nano* **2015**, *9*, 869.
- [42] S. Bhattacharjee, K. L. Ganapathi, D. N. Nath, N. Bhat, *IEEE Trans. Electron Devices* **2016**, *63*, 2556.
- [43] Y. Yin, J. Pang, J. Wang, X. Lu, Q. Hao, E. Saei Ghareh Naz, X. Zhou, L. Ma, O. G. Schmidt, *ACS Appl. Mater. Interfaces* **2019**, *11*, 15891.

- [44] Y. Han, H. Wang, L. Qiang, Y. Gao, Q. Li, J. Pang, H. Liu, L. Han, Y. Wu, Y. Zhang, *J. Mater. Sci.* **2020**, 55, 591.
- [45] D. Somvanshi, S. Kallatt, C. Venkatesh, S. Nair, G. Gupta, J. K. Anthony, D. Karmakar, K. Majumdar, *Phys. Rev. B* **2017**, 96, 205423.
- [46] H. Qiao, Z. Huang, X. Ren, S. Liu, Y. Zhang, X. Qi, H. Zhang, *Adv. Opt. Mater.* **2020**, 8, 1900765.
- [47] Y. Cao, X. Zhu, H. Chen, X. Zhang, J. Zhou, Z. Hu, J. Pang, *Sol. Energy Mater. Sol. Cells* **2019**, 200, 109945.
- [48] Y. B. Xu, H. T. Wang, Y. Tanaka, M. Shimono, M. Yamazaki, *Mater. Trans.* **2007**, 48, 148.
- [49] T. Zhan, Y. Xu, M. Goto, Y. Tanaka, R. Kato, M. Sasaki, *RSC Adv.* **2015**, 5, 49703.
- [50] Y. Xu, R. Kato, M. Goto, *J. Appl. Phys.* **2010**, 108, 104317.
- [51] Y. Xu, M. Goto, R. Kato, Y. Tanaka, Y. Kagawa, *J. Appl. Phys.* **2012**, 111, 084320.
- [52] G. Kresse, J. Hafner, *Phys. Rev. B* **1993**, 47, 558.
- [53] G. F. Kresse, J. Furthmüller, *Comput. Mater. Sci.* **1996**, 6, 15.
- [54] G. F. Kresse, J. Furthmüller, *Phys. Rev. B* **1996**, 54, 11169.
- [55] G. Kresse, J. Hafner, *Phys. Rev. B* **1994**, 49, 14251.
- [56] P. E. Blöchl, *Phys. Rev. B* **1996**, 54, 11169.
- [57] G. Kresse, D. Joubert, *Phys. Rev. B* **1999**, 59, 1758.
- [58] J. P. Perdew, K. Burke, M. Ernzerhof, *Phys. Rev. Lett.* **1996**, 77, 3865.
- [59] E. Scalise, M. Houssa, G. Pourtois, V. Afanas'ev, A. Stesmans, *Nano Res.* **2012**, 5, 43.
- [60] E. R. Jette, F. Foote, *J. Chem. Phys.* **1935**, 3, 605.
- [61] H. J. Monkhorst, J. D. Pack, *Phys. Rev. B* **1976**, 13, 5188.
- [62] G. K. H. Madsen, D. J. Singh, *Comput. Phys. Commun.* **2006**, 175, 67.